Radiated seismic energy based on dynamic rupture models of faulting

Shuo Ma[1] and Ralph J. Archuleta[1]

Received 16 September 2005; revised 12 December 2005; accepted 14 February 2006; published 27 May 2006.

[1] By modeling spontaneous ruptures, we study the mechanism dependence of radiated seismic energy from three hypothetical crustal events, 30° dipping reverse fault, 60° dipping normal fault, and a vertical strike-slip fault, and the 1994 blind-thrust Northridge earthquake. Embedded in a homogeneous half-space, all three hypothetical faults have the same area and are subjected to the same shear and normal stress conditions and frictional parameters. Dynamic simulations produce apparent stress of 0.53 MPa, 0.23 MPa, and 0.34 MPa for the reverse, normal, and strike-slip faults, respectively. The energy distribution on a distant surface shows that a large fraction of energy is concentrated in the forward direction of rupture propagation. We use spontaneous rupture models to compute the radiated energy from the 1994 Northridge earthquake. The initial stress drop distribution is based on a kinematic slip distribution. Using a linear slip-weakening friction law, we modify both the initial stress and yield stress until the dynamic rupture produces near-source synthetics that are consistent with the data. The total radiated seismic energy from our model is 6.0×10^{14} J; seismic moment 1.47×10^{19} Nm; apparent stress 1.5 MPa; fracture energy 3.2×10^{14} J; and slip-weakening distance 0.25 m. The energy flux distribution is heterogeneous with strong directivity effects. These results suggest that correcting for directivity could be difficult, but necessary, for teleseismic and regional estimates of radiated energy. Dynamic source models constrained by ground motions can provide a stable and accurate energy estimate for large earthquakes.

Citation: Ma, S., and R. J. Archuleta (2006), Radiated seismic energy based on dynamic rupture models of faulting, *J. Geophys. Res.*, *111*, B05315, doi:10.1029/2005JB004055.

1. Introduction

[2] The total seismic energy released by an earthquake is one of the most important quantities in seismology. Though intuitively understandable, misconceptions on seismic energy often exist. *Haskell* [1964] gives the most accurate definition of seismic energy as the wave energy transmitted to infinity if an earthquake occurred in an infinite, lossless medium. *Kostrov* [1974] rigorously derived the formulas for calculating seismic energy on the fault and related the seismic energy to seismic radiation through a distant surface enclosing the fault. He demonstrated that the total energy going through an enclosing surface is not the total seismic energy radiated from the fault unless the static work is taken into account when the surface is not far from the fault.

[3] Earlier studies used the empirically derived Gutenberg-Richter relation [*Gutenberg*, 1942; *Gutenberg and Richter*, 1956a, 1956b] to estimate the radiated energy [e.g., *Wyss and Brune*, 1971]. Radiated energy has also been estimated from source-time functions determined by inversion of seismograms [*Kikuchi and Fukao*, 1988] and empirical Green's function deconvolutions [*Venkataraman et al.*, 2002]. The establishment of digital broadband networks has allowed estimates of radiated energy by direct integration of velocity records [e.g., *Boatwright and Choy*, 1986; *Houston*, 1990; *Houston and Kanamori*, 1990; *Kanamori et al.*, 1993; *Singh and Ordaz*, 1994; *Choy and Boatwright*, 1995; *Winslow and Ruff*, 1999; *Pérez-Campos and Beroza*, 2001]. Although the digital networks have improved energy estimates, these estimates are still subject to large uncertainties because source directivity and propagation path effects are difficult to account for accurately.

[4] The underlying principle for the direct estimate of seismic energy from data is that the far-field *P*- and *S*-wave displacement is proportional to the moment rate time history assuming a point source [e.g., *Venkataraman and Kanamori*, 2004]. From the source time function, the radiated energy can be calculated using the relation [e.g., *Vassiliou and Kanamori*, 1982] $E_R = (1/(15\pi^2\rho\alpha^5) + 1/(10\pi^2\rho\beta^5)) \int \omega^2|\dot{M}(\omega)|^2\, d\omega$, where $\dot{M}(\omega)$ is the moment rate source spectrum and the density ρ, *P*-wave velocity α, *S*-wave velocity β are in the source region. To take the observation back to the source, one must correct for attenuation, depth, receiver function and source properties such as directivity and radiation pattern over a wide range of frequencies, all assuming a point source. At teleseismic distances, the *S*-wave is severely attenuated and rarely used. In general, the *P*-wave group (*P*, *pP* and *sP*) is used for the teleseismic estimate of seismic energy [e.g., *Boatwright and*

[1]Department of Earth Science and Institute for Crustal Studies, University of California, Santa Barbara, California, USA.

0148-0227/06/2005JB004055$09.00

Choy, 1986; *Choy and Boatwright*, 1995; *Pérez-Campos and Beroza*, 2001]. For the regional estimates the *S*-wave is used [e.g., *Kanamori et al.*, 1993; *Singh and Ordaz*, 1994; *Boatwright et al.*, 2002]. Different corrections, which can be large, are applied when different data (teleseismic *P*-wave group or *S*-wave) are used. The inherent difficulty in making the corrections accurately is likely a major source of uncertainty in the radiated energy estimate. An order of magnitude difference is common between a teleseismic estimate and a regional estimate for the same earthquake [*Singh and Ordaz*, 1994], which indicates a problem with teleseismic and/or regional estimates of the seismic energy.

[5] *Ide* [2002] presented a different approach from which the radiated energy is directly estimated on the fault. By working directly with the seismic source, the approximations used in the teleseismic and regional energy estimates can be avoided. As *Kostrov* [1974] showed, the basic principle of integrating the energy flux through a closed surface can be applied to the fault surface. By specifying displacement time histories as boundary conditions on the fault, from a kinematic slip model *Ide* [2002] directly computed the shear traction time histories on the fault using a finite difference method. The method is entirely kinematic with the slip function and the rupture velocity specified by the original kinematic model. The stresses are the natural consequences of using the finite difference method. Following Kostrov's approach, he estimated seismic energy for selected earthquakes directly on the fault. However, his estimates are about 3 times lower than estimates from other approaches. This lower estimate might be due to the specification of the slip rate function rather than having this result from the stress change; and/or specification of the rupture velocity, which is nearly constant from linearized inversions; and/or overestimation of fracture energy because the slip weakening distance is nearly equal to the total slip. The omission of abrupt acceleration or deceleration of rupture velocity might lead to a significant error in the energy estimation [*Madariaga*, 1977].

[6] Another approach that estimates the radiated seismic energy directly on the fault uses dynamic rupture models [*Favreau and Archuleta*, 2003]. *Favreau and Archuleta* [2003] only use a kinematic model to determine the initial heterogeneous stress drop on the fault. By trial and error they adjust the yield stress (the stress at which slip initiates) and the slip-weakening distance until the dynamic rupture reproduces seismograms that are consistent with the data. This approach, which we use in this paper, is appealing for many different reasons: first, the dynamics of the faulting process balance all of the energies: potential energy change, fracture energy, frictional heat and radiated energy; second, for many of the large damaging earthquakes there are kinematic models that can be converted into initial models for stress; and third, the radiated seismic energy is almost completely accounted for within the frequency limits of the computation. Although numerical codes that simulate dynamic ruptures are normally limited to frequencies 1.0 Hz and less, this frequency range is sufficient to capture 85–90% of the total energy if the corner frequency of the main shock is on the order of 0.1–0.2 Hz [*Singh and Ordaz*, 1994].

[7] While there are large uncertainties in the seismic energy estimates, they may still provide some important insights into the physics of faulting. One of the striking results found by using teleseismic energy estimates is that the seismic energy released from strike-slip earthquakes is 5–10 times larger than the energy released in thrust faulting. By examining shallow earthquakes with magnitudes $\geq$5.8 that occurred between 1986 and 1991, *Choy and Boatwright* [1995] concluded that the seismic energy released in strike-slip earthquakes is about 10 times the amount in thrust events. This implies that the apparent stress is 10 times greater in strike-slip earthquakes than in thrust events. *Pérez-Campos and Beroza* [2001] examined 204 events worldwide during the period 1992–1999 and reached a similar conclusion: that the seismic energy released from strike-slip earthquakes was greater by about a factor of five compared to thrust events. They find that the apparent stress is on average largest for strike-slip events (0.70 MPa), while for reverse and normal events it is significantly smaller: 0.15 and 0.25 MPa, respectively. However, they pointed out that there is a large discrepancy between the seismic energy estimated by teleseismic data and that from regional data.

[8] These observations are contrary to what one might expect from the state of stress in the crust [*McGarr and Gay*, 1978; *McGarr*, 1980; *Scholz*, 2002]. If one assumes Byerlee's friction law for the limiting strength and a hydrostatic pore pressure gradient, the Anderson theory of faulting would predict the strength of an optimally oriented reverse fault is greater than that of an optimally oriented strike-slip and normal fault. Using a representative depth of 10 km, one would predict the shear strength for a reverse fault is about 2.25 and 3 times larger than that of a strike-slip fault and a normal fault, respectively [see *Scholz*, 2002, Figure 3.27]. Assuming that the initial shear stress on the fault is close to the shear strength and that the sliding friction is equal for each earthquake, this would imply that thrust faulting would have a higher stress drop than either strike-slip or normal faulting earthquakes. If seismic efficiency is the same for the different faulting mechanisms, one might expect the apparent stress to show a similar relationship, namely thrust faulting having the largest apparent stress, followed by strike-slip and then normal faulting.

[9] In this paper, we examine the mechanism dependence of radiated seismic energy from large earthquakes by simulating earthquakes as spontaneous ruptures using the finite element (FE) method. First, we briefly summarize the key steps in the FE modeling of rupture dynamics and derive the energy balance equations in the dynamics of faulting from a mechanical point of view. Then we simulate three hypothetical crustal events: a 30° dipping reverse fault, a 60° dipping normal fault, and a vertical strike-slip fault. All three hypothetical faults have the same area and are subjected to the same shear and normal stress conditions in a homogeneous half-space. Except for the geometry and the mechanism, all other conditions are identical. The main purpose is to see whether or not strike-slip earthquakes radiate 5–10 times more energy than reverse and normal events. Finally, we simulate the dynamic rupture process for the 1994 Northridge earthquake and compare our computed apparent stress for the Northridge earthquake, a thrust earthquake, with the 1979 Imperial Valley earthquake, a

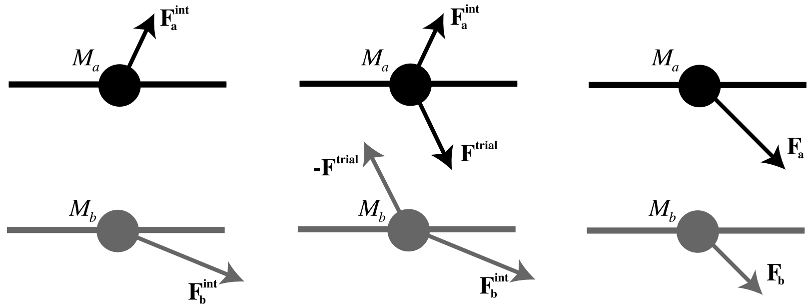

Figure 1. Split nodes are used to represent the two sides of the fault, where the force perturbations on the initial state between the nodes give the external forces on the system. Prior to rupture, a nodal constraint force is applied to ensure that both nodes have the same acceleration.

strike-slip earthquake, modeled by *Favreau and Archuleta* [2003].

2. FE Modeling of Rupture Dynamics and Energy Balance

[10] In the finite element method, after the Galerkin discretization using finite elements in space the equations of motion can be transformed into a system of ordinary differential equations

$$M\ddot{U} + C\dot{U} + F^{\text{int}} = F^{\text{ext}}, \tag{1}$$

where U is the global displacement vector, M is the mass matrix, C is the damping matrix associated with material damping and absorbing boundary conditions, F^{int} is the internal force vector associated with the internal deformation of material, and F^{ext} is the external force vector. When second-order elements (e.g., three-dimensional four-node tetrahedral, six-node wedge and eight-node hexahedral elements) are used, the mass matrix M can be lumped into a diagonal matrix. If simple dampers are used in the absorbing boundaries [*Lysmer and Kuhlemeyer*, 1969] and material damping is ignored, the damping matrix C is also diagonal. These approximations lead to a very efficient central difference scheme for solving the equation (1) because it is unnecessary to invert a large matrix. For simplicity, we use the elementary dampers of *Lysmer and Kuhlemeyer* [1969] for the absorbing boundaries in all the simulations of this paper.

[11] The dynamics of faulting is a mixed boundary value problem. The key to solving it is to find the external forces on the system: the mutual forces between the two sides of the fault. Once the external forces are obtained, solving for the dynamics of faulting reduces to solving for the material response due to applied forces. We summarize briefly the key steps necessary to obtain the external forces in the case of a split node scheme [*Andrews*, 1999].

[12] Two colocated nodes are used to model the dynamics of faulting, with each node representing a small area on one side of fault. The nodes move relative to each other along the fault plane. There is no opening of the fault; nor can one side penetrate the other. The force between the split nodes in the initial equilibrium state is $\mathbf{T_0}$. The force during the faulting is $\mathbf{T}$. M_a and M_b are the masses of the split nodes. $\mathbf{F_a^{int}}$ and $\mathbf{F_b^{int}}$ are the internal forces caused by the deformation on each side of the fault. We calculate a trial force $\mathbf{F^{trial}}$ between the nodes assuming no slip (Figure 1). The node accelerations are given by

$$\mathbf{a_a} = \frac{\mathbf{F^{trial}} + \mathbf{F_a^{int}}}{M_a}$$
$$\mathbf{a_b} = \frac{-\mathbf{F^{trial}} + \mathbf{F_b^{int}}}{M_b}.$$

To ensure collocation we set $\mathbf{a_a} = \mathbf{a_b}$ by applying a force $\mathbf{F^{trial}} = (M_a\mathbf{F_b^{int}} - M_b\mathbf{F_a^{int}})/(M_a + M_b)$ between the nodes.

[13] There are three cases where the force $\mathbf{T}$ is determined differently.

[14] 1. When the absolute force $\mathbf{T_0} + \mathbf{F^{trial}}$ is smaller than the yield force, there is no slip and the absolute force between the nodes is $\mathbf{T} = \mathbf{T_0} + \mathbf{F^{trial}}$.

[15] 2. When the two nodes are slipping, the absolute force between the nodes is the frictional force $\mathbf{f}$, i.e., $\mathbf{T} = \mathbf{f}$. Naturally, the frictional force $\mathbf{f}$ is dependent on the type of friction law employed. In the case of a slip-weakening friction law [*Ida*, 1972], the frictional force $\mathbf{f}$ is only a function of slip, which is known at every time step.

[16] 3. We calculate the healing force $\mathbf{F^{heal}}$ at each time step, which is the force necessary to cause the slip to stop in the next half time step. It can be shown that

$$\mathbf{F^{heal}} = \mathbf{F^{trial}} - \frac{M_a M_b}{M_a + M_b}\frac{\Delta\mathbf{v}}{\Delta t},$$

where $\Delta\mathbf{v}$ is the slip velocity in the previous half time step. If the current frictional force $\mathbf{f}$ is bigger than $\mathbf{T_0} + \mathbf{F^{heal}}$, the slip will stop in the next half time step and the absolute force $\mathbf{T} = \mathbf{T_0} + \mathbf{F^{heal}}$; otherwise, $\mathbf{T} = \mathbf{f}$.

[17] Because we solve the dynamics of faulting based on the perturbation of the initial state $\mathbf{T_0}$, the actual forces between the split nodes in every case must be given by

$$\mathbf{F} = \mathbf{T} - \mathbf{T_0}. \tag{2}$$

These are the external forces applied on the system that essentially give the F^{ext} in equation (1). Once F^{ext} is obtained, equation (1) can be solved. One significant advantage of the split node scheme is that the forces and

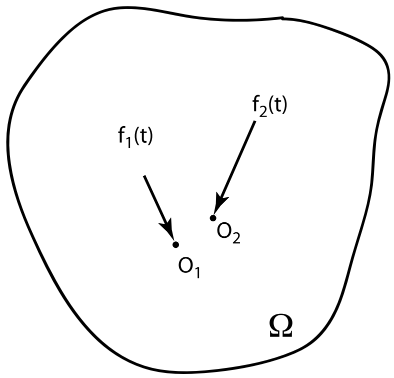

Figure 2. Two external forces are applied to an elastic body that was in equilibrium. If both forces are transient, they will both be the energy sources, and the radiated energy partition between the two forces is well determined. If both forces are nontransient and the material response at one point is affected by the force at the other point, the static field will prevent differentiating the radiated energy between the two forces. Therefore both forces are energy sources; however, the exact energy partition cannot be determined. If the static field caused by one force is significantly smaller than the other, an approximation of radiated energy partition can be obtained.

velocities are colocated at the nodes, i.e., the two critical frictional variables, the tractions on the fault and the slip rate, are computed at the same location. We refer to *Andrews* [1999] for more details on the split node scheme.

[18] *Kostrov* [1974] has rigorously derived the energy balance equations for the dynamics of faulting. In the following, we derive the energy balance equations from a mechanical point of view. It is less rigorous, but very helpful to clarify some of the concepts related to seismic energy.

[19] Suppose $\mathbf{f_1}(\mathrm{t})$ is an external force at point O_1 on an elastic body that was in equilibrium and $\mathbf{v_1}(\mathrm{t})$ is the velocity response at point O_1. Then the total work done by $\mathbf{f_1}(\mathrm{t})$ is defined as $W_{\mathrm{total}} = \int_0^\infty \mathbf{f_1}(\mathrm{t}) \cdot \mathbf{v_1}(\mathrm{t})dt$. If the force $\mathbf{f_1}(\mathrm{t})$ is transient, i.e., associated with no permanent deformation, W_{total} is the total radiated energy. In this case, all of the work is radiated as waves. However, if $\mathbf{f_1}(\mathrm{t})$ is not transient, the final constant force $\mathbf{f_1}(\infty)$ is permanently applied to the system. It will cause a static field, where the final displacement at point O_1 is $\mathbf{u_1}$ (note $\mathbf{u_1} = \int_0^\infty \mathbf{v_1}(t)dt$), and the total static work caused by $\mathbf{f_1}(t)$ will be $W_{\mathrm{static}} = (1/2)\mathbf{f_1}(\infty) \cdot \mathbf{u_1}$. The total radiated energy is given by $E_R = W_{\mathrm{total}} - W_{\mathrm{static}}$, i.e., the total work consists of both the radiated energy and the static work. The force $\mathbf{f_1}(\mathrm{t})$ is the only energy source. If there is a second nontransient force $\mathbf{f_2}(\mathrm{t})$ applied at a nearby location (Figure 2), then $\mathbf{f_1}(\mathrm{t})$ and $\mathbf{f_2}(\mathrm{t})$ will both be the energy sources. However, there is no way to determine the partitioning of energy between $\mathbf{f_1}(\mathrm{t})$ and $\mathbf{f_2}(\mathrm{t})$ if the velocity $\mathbf{v_1}(\mathrm{t})$ is affected by the other force $\mathbf{f_2}(\mathrm{t})$ and vice versa. Because both forces contribute to the static field, the static field caused by one force contributes to the total work done by the other force through the velocity response; thus the contributions from the two forces to the total work cannot be differentiated. Thus the radiated energy partition cannot be made. The total radiated energy, however, is uniquely determined. We will use this important concept later. If $\mathbf{f_1}(\mathrm{t})$ and $\mathbf{f_2}(\mathrm{t})$ are both transient, there is no static field. Even though the other force affects the velocity response, the radiated energy partition is uniquely determined by the total work done by $\mathbf{f_1}(\mathrm{t})$ and $\mathbf{f_2}(\mathrm{t})$, respectively.

[20] As we have shown previously in the dynamics of faulting, the external forces are related to the traction change on the fault (see equation (2)), i.e., the stress change $\boldsymbol{\Delta\sigma}(\boldsymbol{\xi}, t) = \boldsymbol{\sigma}(\boldsymbol{\xi}, t) - \boldsymbol{\sigma}_0(\boldsymbol{\xi})$ multiplied by area. In the following all $\boldsymbol{\sigma}$ refer to shear stresses. If we apply the same concept to the fault $\sum$, the total work done by the stress change $\boldsymbol{\Delta\sigma}(\boldsymbol{\xi}, t)$ is

$$
\begin{aligned}
W_{\mathrm{total}} &= \int_0^\infty \int_\Sigma -\boldsymbol{\Delta\sigma}(\boldsymbol{\xi}, t) \cdot \mathbf{v_a}(\boldsymbol{\xi}, t) d\boldsymbol{\Sigma} dt \\
&\quad + \int_0^\infty \int_\Sigma \boldsymbol{\Delta\sigma}(\boldsymbol{\xi}, t) \cdot \mathbf{v_b}(\boldsymbol{\xi}, t) d\boldsymbol{\Sigma} dt \\
&= \int_0^\infty \int_\Sigma -\boldsymbol{\Delta\sigma}(\boldsymbol{\xi}, t) \cdot \boldsymbol{\Delta}\mathbf{v}(\boldsymbol{\xi}, t) d\boldsymbol{\Sigma} dt,
\end{aligned}
$$

where $\mathbf{v_a}(\boldsymbol{\xi}, t)$ and $\mathbf{v_b}(\boldsymbol{\xi}, t)$ represent the particle velocities of each side of the fault, and the slip velocity is $\boldsymbol{\Delta}\mathbf{v}(\boldsymbol{\xi}, t) = \mathbf{v_a}(\boldsymbol{\xi}, t) - \mathbf{v_b}(\boldsymbol{\xi}, t)$. Using $\boldsymbol{\Delta\sigma}(\boldsymbol{\xi}, t) = \boldsymbol{\sigma}(\boldsymbol{\xi}, t) - \boldsymbol{\sigma}_0(\boldsymbol{\xi})$, then

$$
W_{\mathrm{total}} = \int_\Sigma \boldsymbol{\sigma}_0(\boldsymbol{\xi}) \cdot \boldsymbol{\Delta}\mathbf{u_1}(\boldsymbol{\xi}) d\boldsymbol{\Sigma} - \int_0^\infty \int_\Sigma \boldsymbol{\sigma}(\boldsymbol{\xi}, t) \cdot \boldsymbol{\Delta}\mathbf{v}(\boldsymbol{\xi}, t) d\boldsymbol{\Sigma} dt, \tag{3}
$$

where $\boldsymbol{\sigma}_0(\boldsymbol{\xi})$ is the initial stress; $\boldsymbol{\sigma}(\boldsymbol{\xi}, t)$ is the stress during the faulting, and $\boldsymbol{\Delta}\mathbf{u_1}(\boldsymbol{\xi})$ is the final slip. The total static work done by the stress change is given by

$$
\begin{aligned}
W_{\mathrm{static}} &= \frac{1}{2} \int_\Sigma -\boldsymbol{\Delta\sigma}(\boldsymbol{\xi}, \infty) \cdot \boldsymbol{\Delta}\mathbf{u_1}(\boldsymbol{\xi}) d\boldsymbol{\Sigma} \\
&= \frac{1}{2} \int_\Sigma [\boldsymbol{\sigma}_0(\boldsymbol{\xi}) - \boldsymbol{\sigma}_1(\boldsymbol{\xi})] \cdot \boldsymbol{\Delta}\mathbf{u_1}(\boldsymbol{\xi}) d\boldsymbol{\Sigma},
\end{aligned} \tag{4}
$$

where $\boldsymbol{\sigma_1}(\boldsymbol{\xi})$ is the final stress. Thus the total radiated energy is given by

$$
\begin{aligned}
E_R = W_{\mathrm{total}} - W_{\mathrm{static}} &= \int_\Sigma \frac{\boldsymbol{\sigma}_0(\boldsymbol{\xi}) + \boldsymbol{\sigma}_1(\boldsymbol{\xi})}{2} \cdot \boldsymbol{\Delta}\mathbf{u_1}(\boldsymbol{\xi}) d\boldsymbol{\Sigma} \\
&\quad - \int_0^\infty \int_\Sigma \boldsymbol{\sigma}(\boldsymbol{\xi}, t) \cdot \boldsymbol{\Delta}\mathbf{v}(\boldsymbol{\xi}, t) d\boldsymbol{\Sigma} dt.
\end{aligned} \tag{5}
$$

[21] This is a commonly used formula for calculating the radiated energy. The first term is sometimes called the potential energy change including both the gravity and strain energy change. The second term is the total energy

t1.1 **Table 1.** Three-Dimensional Calculation Parameters for the Hypothetical Models

	Parameter	Value
t1.2	Parameter	Value
t1.3	Initial shear stress, MPa	17.75
t1.4	Normal stress, MPa	30
t1.5	Static friction coefficient	0.64
t1.6	Dynamic friction coefficient	0.525
t1.7	Critical slip-weakening distance, m	0.6
t1.8	Radius of initial patch, km	3
t1.9	Homogeneous half-space	
t1.10	V_p, m/s	5190
t1.11	V_s, m/s	3000
t1.12	ρ, kg/m^3	2700

loss during faulting and consists of both the fracture energy and the frictional heat. If we integrate equation (5) by parts, we obtain

$$E_R = \int_{\Sigma} \frac{\boldsymbol{\sigma}_0(\boldsymbol{\xi}) - \boldsymbol{\sigma}_1(\boldsymbol{\xi})}{2} \cdot \boldsymbol{\Delta}\mathbf{u_1}(\boldsymbol{\xi}) d\boldsymbol{\Sigma} + \int_0^{\infty} \int_{\Sigma} \dot{\boldsymbol{\sigma}}(\boldsymbol{\xi}, t) \cdot \boldsymbol{\Delta}\mathbf{u}(\boldsymbol{\xi}, t) d\boldsymbol{\Sigma} dt. \tag{6}$$

This is the formula *Kostrov* [1974] derived. Note that in this formula the radiated energy does not depend on the absolute stress level as, in fact, it should not. *Favreau and Archuleta* [2003] showed that the second term contains both the fracture work and the relaxation work.

[22] If we apply the same concept to a distant surface S enclosing the source, then the total work done by seismic waves against S is

$$W_{\text{total}} = \int_0^{\infty} \int_S -\tau_{ij} \dot{u}_i n_j dS dt, \tag{7}$$

where τ_{ij} is the stress perturbation on the surface S caused by waves, $\dot{u}_i$ is the velocity field, and n_j is the outer normal of S. The static work is given by

$$W_{\text{static}} = -\frac{1}{2} \int_S \tau_{ij}^1 u_i^1 n_j dS, \tag{8}$$

where τ_{ij}^1 is the final stress perturbation and u_i^1 the final displacement. The radiated energy is given by $E_R = W_{\text{total}} - W_{\text{static}}$. The total amount of radiated energy from the fault should be equal to the total radiated energy through the surface S for the conservation of energy; this provides a stringent test for the numerical calculations.

[23] As was shown earlier, if the static work is not negligible compared to the total work, then there is no way to determine the amount of energy radiated from each energy source separately. Consequently, there can be no map of radiated energy density on the fault [e.g., *Ide*, 2002; *Favreau and Archuleta*, 2003] because the static work on the fault (equation (4)) is never negligible. *Rivera and Kanamori* [2005] also objected to interpreting maps of radiated energy density being made by subtracting the energy lost to fracture and frictional heat from the elastic potential energy change. They showed that such maps are nonunique, also acknowledged by *Favreau and Archuleta* [2003]. We here would argue that a map of radiated energy density on the fault does not exist because the contribution of the static field cannot be partitioned to separate areas of the fault. However, these maps [*Ide*, 2002; *Favreau and Archuleta*, 2003] could be interpreted as the net work done to the volume by the stress change on the fault. A negative net work on the fault does not mean this part of fault does not radiate; every point on the fault that slips radiates energy. It simply means the work done to the volume is less than the work taken from the volume on this part of fault. *Fukuyama* [2005] introduced a new term "radiation energy" to define the total work in equation (3). In this case, radiation energy can be mapped onto the fault. However, by ignoring the static work, a nonnegligible part of the total work, the radiation energy is not a good approximation of the radiated energy. For the same reason, the distribution of radiated energy on a surface S cannot exist unless the surface is far enough from the fault so that the static field on S (equation (8)) is negligible.

3. Radiated Energy for Three Hypothetical Fault Mechanisms

[24] To study the mechanism dependence of seismic energy we modeled dynamic ruptures for three different mechanisms on three hypothetical faults: a 30° dipping reverse fault, a 60° dipping normal fault and a vertical strike-slip fault. The 30° dipping reverse fault and 60° dipping normal fault has the same dimension: 18 km along strike by 24 km along dip. The vertical strike slip fault is 36 km along strike and 12 km along dip. All three faults are subjected to the same shear and normal stress conditions and the same frictional parameters (Table 1) with the use of a linear slip-weakening friction law [*Ida*, 1972]. The initial stress is up dip for the dip-slip earthquakes and along strike for strike-slip earthquake. If there were no variation in the normal stress, the dynamic stress drop (difference between initial and sliding friction stress) would be 2 MPa. Slip is constrained in the initial stress direction, i.e., rake rotation is not allowed. An imposed stress drop of 3.84 MPa on a 3-km-radius circular patch in the lower-right quadrant of the faults nucleates all ruptures.

[25] We used hexahedral elements for the strike-slip earthquake and wedge elements for the dip-slip earthquakes. We simulate waves up to 1 Hz. To model the boundary conditions for faulting, we applied a split node scheme [*Andrews*, 1999]. The rupture spontaneously spreads over the fault. We calculate the work done by seismic waves going through a 45-km-radius hemisphere surrounding the fault for all three events. The simulations are run long enough until all the waves have passed the hemisphere and the system is in equilibrium.

[26] In Figure 3, we plot the rupture time for the three earthquakes. All of the ruptures remain subshear. Rupture propagates faster in the mode II direction than the mode III

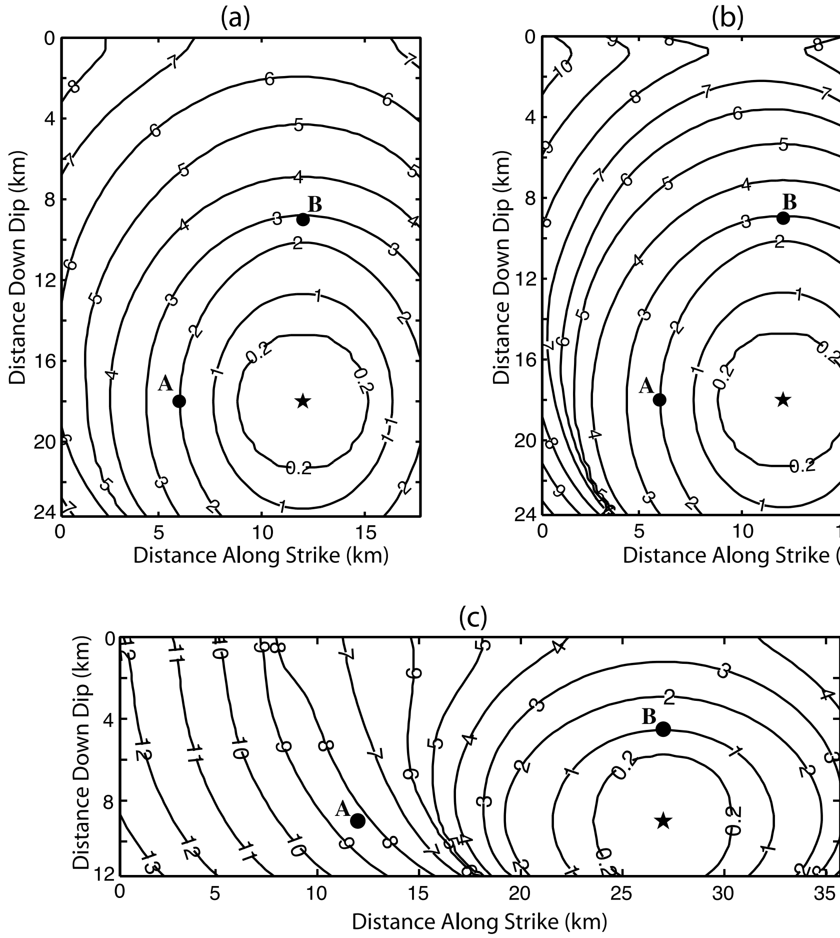

Figure 3. Plot of rupture time on the fault plane for (a) 30° reverse fault, (b) 60° normal fault, and (c) vertical strike-slip fault. Note the locations of points A and B, for which we will show the time histories and slip weakening behavior in Figures 4, 5, and 6.

direction. Also, all three ruptures break the free surface. The stress conditions in Table 1 were carefully chosen so that rupture does not jump to a supershear speed when it breaks the surface for the strike-slip earthquake. In Figures 4, 5, and 6, we depict the time histories of the shear stress, slip rate, and shear stress as a function of slip at two specific points (A and B shown in Figures 3a, 3b, and 3c) for the three earthquakes. The second and third pulses in the slip rate plot correspond to the reflected phases after rupture breaks the surface. The shear stress rises from the initial stress to the yield stress and then breaks down in a linear slip-weakening fashion to the dynamic friction. When the slip stops, restrengthening or relaxation occurs that changes the shear stress from dynamic friction to an either higher or lower final stress. The restrengthening or relaxation, the process to achieve the final equilibrium, is important in the balance of energy because the final stress is a parameter in the equations (5) and (6). Note that for dip-slip earthquakes, the dynamic friction variations are caused by the normal stress variation created by waves reflecting from the free surface [*Oglesby et al.*, 1998].

[27] We found that reverse faulting has a larger moment (1.95×10^{19} Nm) compared to the normal and strike-slip faulting (1.27×10^{19} Nm and 1.14×10^{19} Nm, respectively). The thrust fault radiates much more energy (4.23×10^{14} J) than the normal and strike-slip faults (1.19×10^{14} J and 1.58×10^{14} J, respectively) even if the radiated energy is scaled for the difference in seismic moment. This is contrary to the results found from teleseismic estimates. The apparent stresses for the hypothetical reverse fault, normal fault and strike-slip fault are 0.53 MPa, 0.23 MPa, and 0.34 MPa, respectively (Table 2).

[28] The distribution of energy flux on the 45-km-radius hemisphere surrounding each fault for the reverse, normal and strike-slip events is shown in Figures 7, 8, and 9, respectively. The radiated energy on the sphere is 100%, 97% and 100% of the total radiated energy on the fault for the 30° reverse fault, 60° normal fault and vertical strike-slip fault, respectively (Table 2). The total static work on the sphere is 2.61%, 4.65%, and 5.00% of the total work done by seismic waves for the 30° reverse fault, 60° normal fault and vertical strike-slip fault, respectively. Therefore the static work is negligible and the distribution of energy flux can be mapped onto the surface of the hemisphere. Directivity is dramatic for the 30° reverse and the vertical strike-slip faults (Figures 7 and 9, respectively). A large portion of energy propagates near the surface in the forward direction of propagation. Very little energy goes out of the bottom of

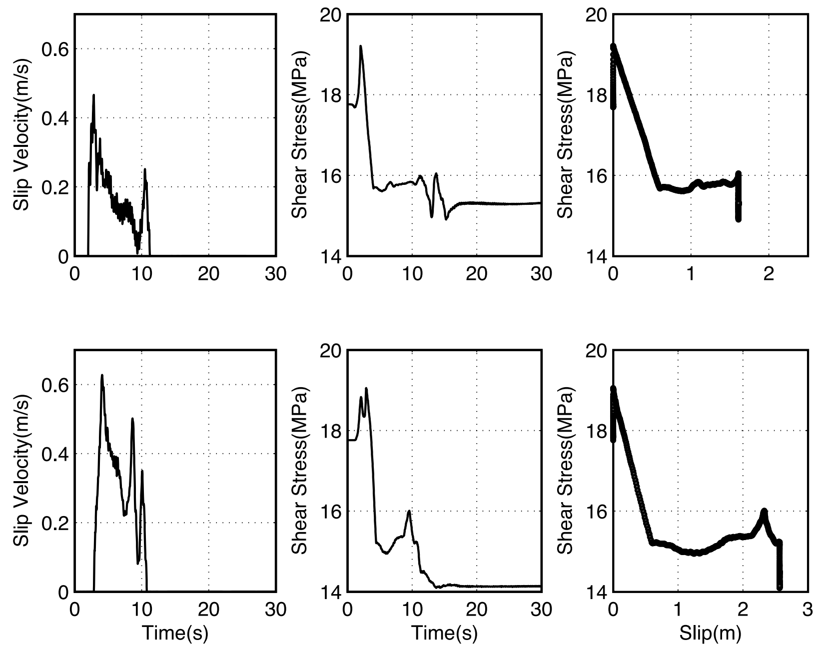

Figure 4. Plots of time histories of slip rate (first column) and shear stress (second column) and shear stress versus slip (third column) for the two points, A and B, on the 30° reverse fault. The top and bottom row correspond to the points A and B in Figure 3, respectively. Note the stress changes from the dynamic friction to a higher or lower final stress when the slip stops. This is an important process in the balance of energy.

the hemisphere. The directivity effect is less dramatic for the 60° normal fault (Figure 8). However, large energy fluxes can still be seen in both the forward and backward direction of rupture propagation. The small cone of large concentration of radiated energy at a deep angle on the hemisphere (Figure 8) might be due to the large stress drop in the nucleation because the cone coincides with the normal projection of the hypocenter on the hemisphere. A similar patch can be seen on the hemisphere for the reverse fault (Figure 7).

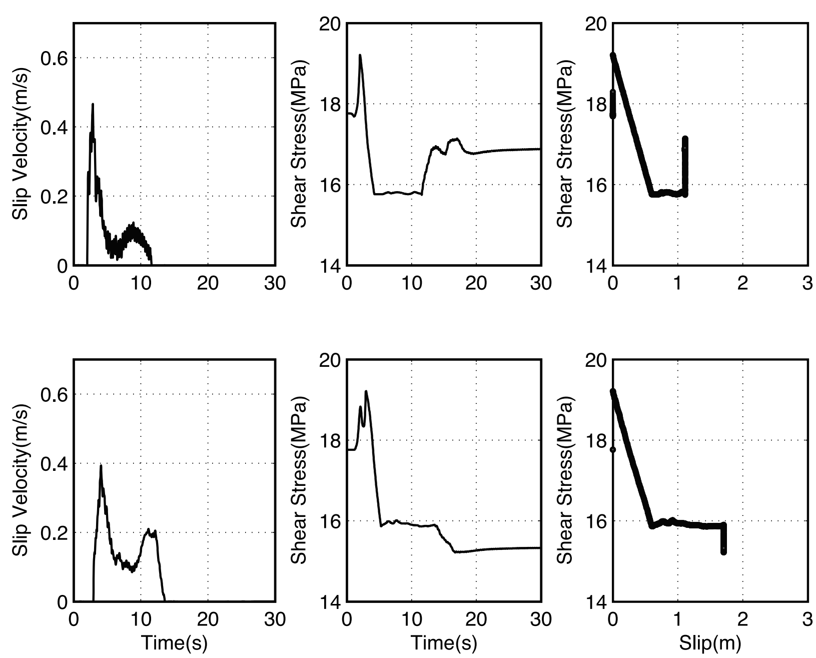

Figure 5. These plots are similar to those in Figure 4 except for the 60° normal fault.

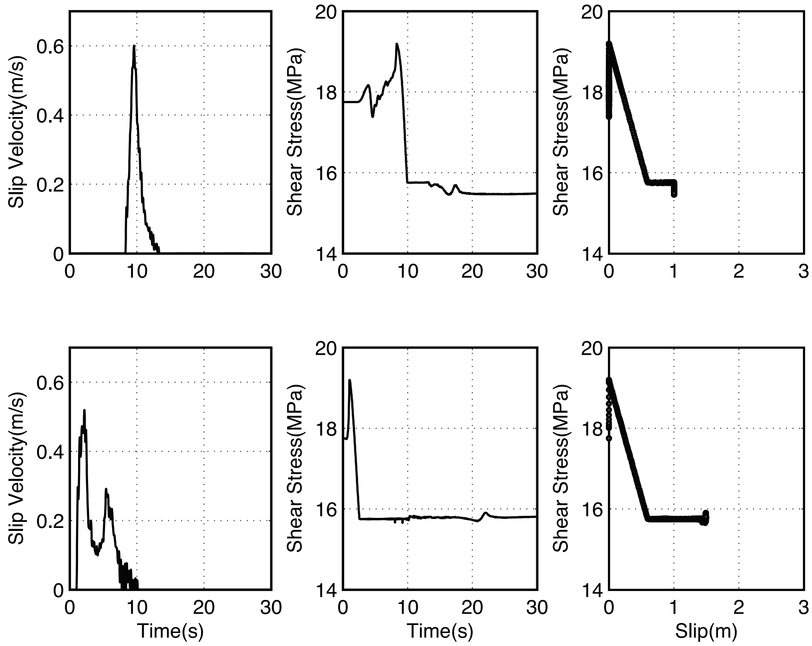

Figure 6. These plots are similar to those in Figure 4 except for the vertical strike-slip fault.

[29] In our simulations reverse faulting has the greatest apparent stress followed by strike-slip faulting with normal faulting having the smallest apparent stress. This is consistent with the state of stress if all earthquakes occur in the same tectonic environment, but this result is not consistent with the energy estimates based on teleseismic observations (Table 3). We realize that we have assumed the same initial shear stress conditions on the fault for all three mechanisms in order to have nearly the same average stress drop for the different mechanisms [*Kanamori and Anderson*, 1975]. However, we expect that the apparent stress differences between the reverse faulting and the normal and strike-slip faulting will be greater if the stress drop were proportional to the state of the stress. Our results are consistent with the findings of *McGarr* [1999] and *Choy and McGarr* [2002] who showed that the apparent stress is directly related to and limited by fault strength.

[30] Our hypothetical models are very simplified earthquake rupture models without the complexities of real earthquakes, such as pore pressure, tectonic environment, etc. The simplicity in the models (the only differences among the three hypothetical events are the style of faulting and geometry) allows us to examine if apparent stress is mechanism-dependent. Our apparent stress results have a mechanism dependence that happens to be coincident with the state of stress in the crust. The numerical results are not consistent with the observations and suggest that the dependence of apparent stress on mechanism found in the observations has a different underlying cause.

[31] The uncertainty for the current energy estimates is large. Indeed, as our simulations demonstrate, the energy going to teleseismic distances is only a very small percentage of the total radiated energy during an earthquake. Because the energy distribution associated with different take-off angles is heterogeneous, it is very difficult to estimate accurately the total radiated energy by extrapolating it from only a small part of the focal sphere.

[32] One possible explanation for the mechanism dependence of apparent stress based on teleseismic observations is that the seismic energy going to teleseismic distances is itself mechanism-dependent [*Pérez-Campos and Beroza*, 2001]. While the energy flux for the three events has been plotted on the surface of a sphere far from the fault, the

t2.1 **Table 2.** Results of 3-D Dynamic Modeling for Three Prototype Focal Mechanisms

		Reverse Fault 30°	Normal Fault 60°	Strike-Slip 90°
t2.2				
t2.3	Fault			
t2.4	Radiated energy, J	4.23×10^{14}	1.19×10^{14}	1.58×10^{14}
t2.5	Seismic moment, Nm	1.95×10^{19}	1.27×10^{19}	1.14×10^{19}
t2.6	Apparent stress, MPa	0.53	0.23	0.34
t2.7	Sphere			
t2.8	Total work, J	4.35×10^{14}	1.20×10^{14}	1.65×10^{14}
t2.9	Static work, J	1.13×10^{13}	5.58×10^{12}	8.27×10^{12}
t2.10	Static work/total work, %	2.61	4.65	5.00
t2.11	Radiated energy, J	4.24×10^{14}	1.14×10^{14}	1.57×10^{14}
t2.12	Radiated energy on sphere/radiated energy on fault	1.00	0.97	1.00

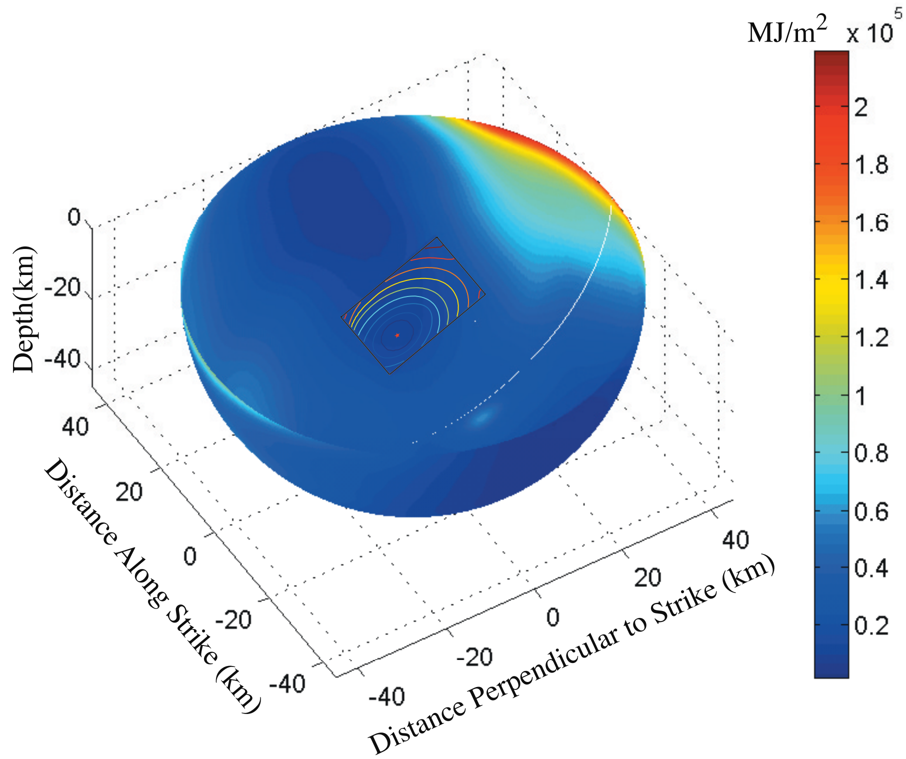

Figure 7. Energy flux distribution on a 45 km radius hemisphere surrounding the 30° reverse fault and rupture time contours on the fault. The star is the hypocenter. The origin of the hemisphere is the surface projection of the geometrical center of the fault. A large proportion of radiated energy is concentrated in the forward direction of rupture propagation, demonstrating the effect of rupture directivity. Energy going to teleseismic distances (energy leaving near the bottom part of the hemisphere) is small.

exact partition of the energy going to teleseismic distances in these cases cannot be done. This can be explained by looking at Figure 10. Teleseismic waves are normally associated with takeoff angles 18° ~ 25° [*Venkataraman and Kanamori*, 2004]. The area associated with teleseismic waves radiated from a point on the fault is well determined on the sphere. Because each point on the fault that slips radiates, the energy going through the same area, however, should include all the contributions from other points on the fault that have takeoff angles other than 18° ~ 25°. Only when the surface of the sphere is sufficiently distant such that the fault can be approximated by a point source, can such energy partition be done. However, we can imagine as the surface of sphere moves farther away from the fault, the energy distribution would not change dramatically. Therefore the energy going to teleseismic distances in the three hypothetical models is likely to be small.

4. Dynamic Modeling of the Northridge Earthquake and Its Radiated Energy

[33] In order to compare radiated energy from two similar-sized crustal earthquakes with different mechanisms, we dynamically simulate the rupture propagation of the 1994 M_w 6.7 Northridge blind-thrust earthquake and estimate its radiated energy. We compare the energy-to-moment ratio with that of the M_w 6.6 Imperial Valley strike-slip earthquake [*Favreau and Archuleta*, 2003].

[34] The 17 January 1994 Northridge earthquake is a particularly significant event because of its location (metropolitan Los Angeles), large well-recorded ground motions, and extensive damage. Several excellent studies of the rupture process have been completed using different data sets and approaches [*Dreger*, 1994; *Zeng and Anderson*, 1996; *Wald et al.*, 1996; *Hartzell et al.*, 1996]. For example, *Wald et al.* [1996] combined geodetic data and teleseismic data with strong ground motion data to retrieve the kinematic rupture history. *Hartzell et al.* [1996] used a hybrid global search algorithm to simultaneously invert for the slip amplitude, rise time, rake and rupture time on the fault. *Day et al.* [1998] and *Bouchon* [1997] determined the space-time variation of shear stress on the fault from kinematic slip models.

[35] Generally, previous attempts at modeling the Northridge earthquake have been kinematic, which contain some mechanical inconsistencies. In kinematic models, the rupture is forced to propagate more or less within a certain predetermined range of speeds. The evolution of slip with time is assumed to follow certain functional forms. Dynamic models, on the other hand, are physically based. The motion of the rupture front and slip time histories are determined from the simultaneous control of the stress drop and rupture

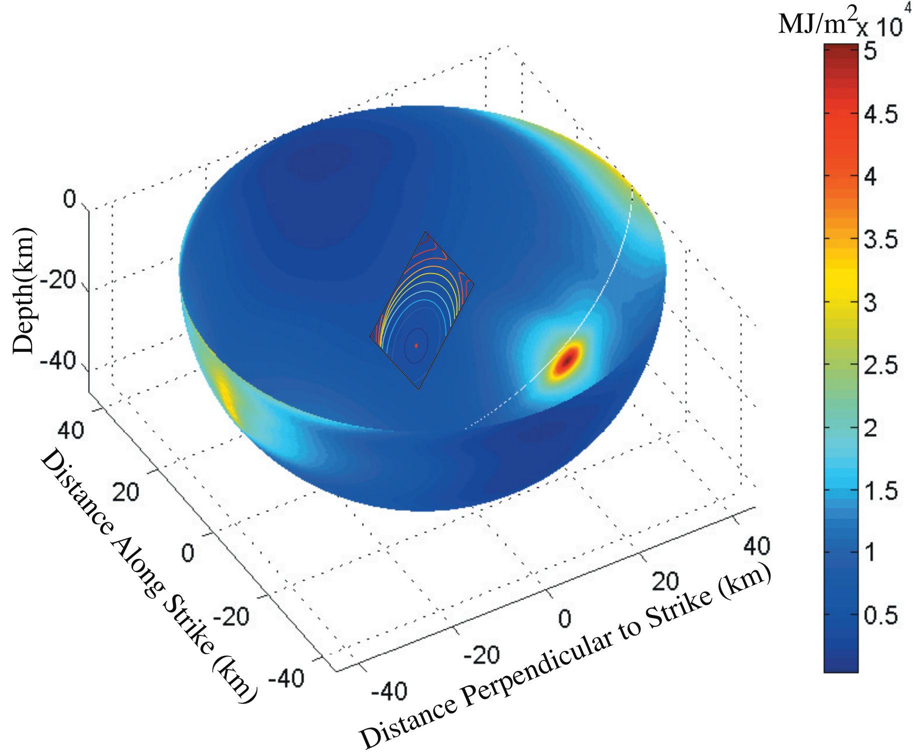

Figure 8. Energy flux distribution on a 45 km radius hemisphere surrounding the 60° normal fault and rupture time contours on the fault. The star is the hypocenter. The origin of the hemisphere is the surface projection of the geometrical center of the fault. Rupture directivity is less obvious with concentrations of radiated energy observed in both the forward and backward direction of rupture propagation. The small cone of large energy flux concentration at a deep angle on the sphere is due to the large stress drop in the nucleation.

resistance by friction. *Nielsen and Olsen* [2000] presented a dynamic rupture model for the Northridge earthquake; however their synthetics do not match the data all that well. In the following, we present a data-consistent spontaneous rupture model for the Northridge earthquake from which we estimate the radiated energy.

[36] To set the initial stress field, we use the kinematic slip model from *Hartzell et al.* [1996]. By ensuring the continuity of tractions across the fault, we calculate the static stress drop distribution on the fault by a static FE method. The fault is modeled as a planar fault that is 20 km along strike and 24.89 km down dip; the fault strikes 122° and dips 40°. The top of the fault is 5 km deep. The hypocenter is 17.47 km deep. The fault is embedded in the same layered velocity structure (Table 4) that is used for the rupture dynamic simulations. Because the stress drop is related to the spatial derivative of the slip field, the calculated stress drop distribution on the fault is noisy. We smoothed the stress drop distribution with a ∼1.5 km running average over the fault plane. An arbitrary stress level of 18 MPa is added to the stress drop to obtain the initial stress field. This initial stress field serves only as a starting model and will be modified in order to generate a rupture process that can generate synthetics that match the data. We assume a constant normal stress of 60 MPa over the entire fault; this imposes a uniform dynamic friction coefficient of 0.3 over the fault. For the friction law, we use a constant slip-weakening friction law [*Ida*, 1972]. We assume a uniform critical slip-weakening distance (D_c) on the fault. By trying different D_c, we found D_c = 0.25 m provides the best fit to the data.

[37] Using trial and error, we modified both the initial stress obtained previously and the yield stress until the dynamic rupture generated the synthetic particle velocities that matched the near-source data. This is a tedious process. After dozens of dynamic models, we found the distribution of the stress drop and strength excess (the yield shear stress minus initial shear stress) (Figure 11). The stress drop distribution is similar to the final slip distribution of *Hartzell et al.* [1996]. High stress drops coincide with regions where high slips occur. Negative or low stress drops between these regions or near the edge of the fault are necessary to keep slip localized. An imposed stress drop of 2 MPa on a 1.5-km-radius circular patch surrounding the hypocenter (Figure 11b) initiates the rupture. Because the initial stress and yield stress vary independently, the strength excess distribution is also heterogeneous.

[38] We spontaneously rupture the fault and calculate the work done by seismic waves on a 30-km-radius hemisphere surrounding the fault in the same layered structure (Table 4) used to calculate the stress-drop distribution. This velocity structure corresponds to rock sites *Hartzell et al.* [1996] used in their inversion. The minimum shear wave velocity is 1000 m/s. Because we are mainly concerned with direct phases of *S*-waves, we think that a layered velocity structure should be sufficient though we realize that many stations are

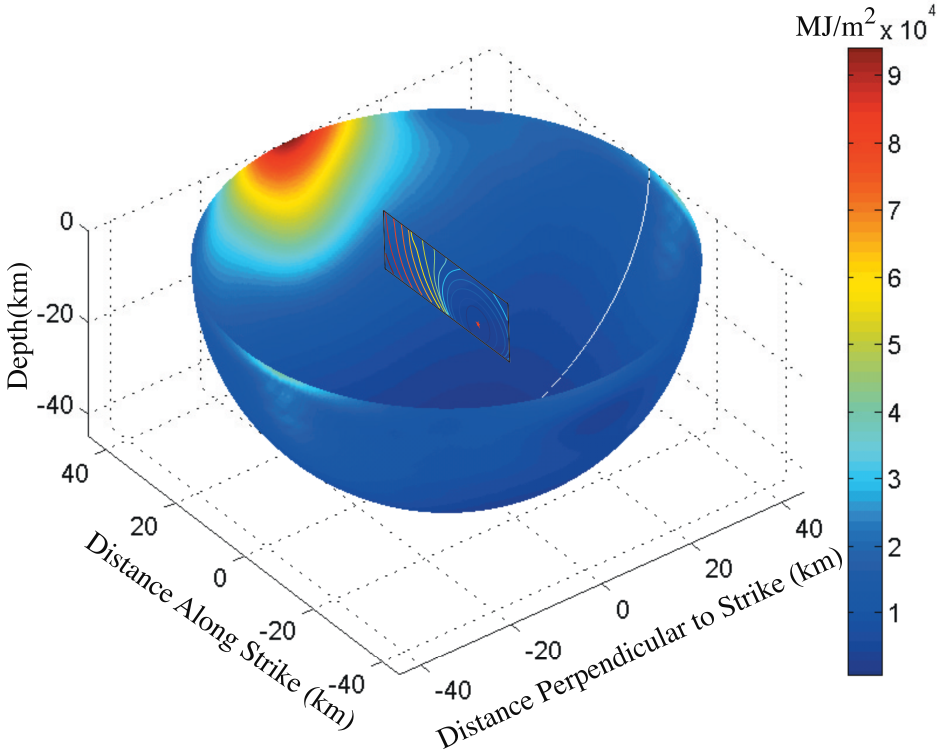

Figure 9. Energy flux distribution on a 45 km radius hemisphere surrounding the vertical strike-slip fault and rupture time contours on the fault. The star is the hypocenter. The origin of the hemisphere is the surface projection of the geometrical center of the fault. A large proportion of radiated energy is concentrated in the forward direction of rupture propagation, making the effect of rupture directivity obvious. Seismic energy leaving at small takeoff angles and going to teleseismic distances is small.

on sediments with shear wave velocities ~400 m/s. We use uniform wedge elements exclusively in our FE code; the dimensions of each element are 119.18 m × 100 m × 100 m. We calculate seismic waves up to 1 Hz in order to capture ~86% of the total energy. The time step is 0.01 s. We carry the simulation for 30 s so that all the waves have passed the hemisphere, and the volume within the hemisphere has reached its final equilibrium state.

[39] In Figure 12 we show snapshots of the dynamic rupture process every 0.75 s. For simplicity, the slip direction is constrained up dip, i.e., pure thrust. Rupture propagates slowly up and eastward soon after initiation. After 3 s, it appears that the rupture almost dies out. However, soon afterward, the rupture front suddenly accelerates and splits (labels A and B). Rupture front A continues to propagate upward and eastward. Rupture front B propagates back down and westward on the fault. About 5 s after origin, the slip rate intensifies on the rupture front (labeled C) in the northwestern part of the fault. The regions of high slip rate, A and C, merge and the rupture terminates on the shallow northwestern part of the fault around 8 s after origin, in agreement with the kinematic inversion. The rupture shows a confined band of slip, which is due to the geometrical heterogeneity of the stress field as suggested by *Beroza and Mikumo* [1996] and *Day et al.* [1998]. Although *Nielsen and Olsen* [2000] included a rate-weakening component in the friction to generate a pulse-like rupture for the Northridge earthquake, this is not necessary in our dynamic model. The final slip distribution is shown at 9 s (Figure 12). The final slip distribution is similar to that from the kinematic inversion; this is not surprising because the initial stress is derived from the kinematic slip model. The spontaneous rupture model gives a seismic moment 1.47×10^{19} Nm, corresponding to M_w 6.7.

[40] The propagation of the rupture front can also be observed in the temporal variation of shear stress on the fault. The rupture front propagation is determined by the immediate history of rupture and by the state of stress at all

t3.1 **Table 3.** Comparison of Ratios of Apparent Stresses and Ratio of State of Stresses

		Reverse/Strike-Slip	Reverse/Normal	Normal/Strike-Slip
t3.2				
t3.3	*Choy and Boatwright* [1995]	0.09	0.64	0.13
t3.4	*Pérez-Campos and Beroza* [2001]	0.21	0.60	0.36
t3.5	This study	1.56	2.3	0.68
t3.6	*Scholz* [2002] state of stress	~2.25	~3	~0.75

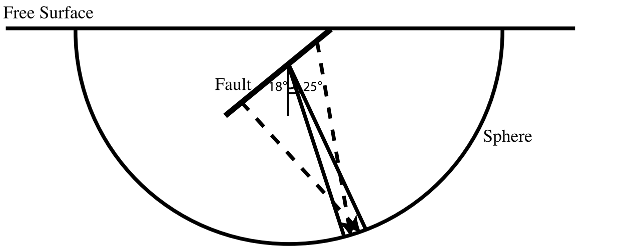

Figure 10. A schematic showing that the energy going to teleseismic distances cannot be determined if the fault dimension is not small compared to the sphere. Because each point on the fault that slips radiates energy, the energy going through a small area on the sphere is associated with many different takeoff angles other than 18° ~ 25°. For simplicity the rays are plotted as straight lines.

nearby points. The passage of rupture front is associated with a stress decrease (green). The rupture tends to propagate into regions of high stress (red), where the high stress drops facilitate the growth of rupture. A strong connectivity of high stress patches is required in order to promote rupture propagation from the initial nucleation point to the remaining parts of the fault [*Nielsen and Olsen*, 2000; *Peyrat et al.*, 2001].

[41] The heterogeneous rupture propagation and stress drop in our model of the Northridge earthquake generates strong seismic radiation. The near-source strong motion stations (Table 5) provide a unique data set for constraining the source characteristics (Figure 13). In Figure 14 we compare the observed ground velocities and the synthetics from our best-fitting dynamic model. All synthetics and data are band-pass filtered between 0.1 and 1.0 Hz with a zero-phase, fourth-order Butterworth filter. We use the same scale for all stations, so that the rupture directivity of the source can be clearly seen. Our synthetics match both the amplitudes and phases well for most stations. A better fit is obtained for stations in the forward direction of rupture propagation (NHL, SYL, SCS, PIRU) and stations close to the hypocenter (ARL, U06, SVA). Our synthetics overpredict the amplitudes at stations in the backward direction (ENR, SCC). At stations U56, SSU and ECC there are unexplained mismatches that might be due to a constrained rake. Overall the data are reasonably reproduced by the synthetics, implying that our dynamic model captures many of the essentials of the true rupture model.

[42] With this dynamic rupture model for the Northridge earthquake, we calculate the radiated energy using equation (5). The radiated energy for the Northridge earthquake is 6.0×10^{14} J. The apparent stress is 1.5 MPa. The total fracture energy is 3.2×10^{14} J, about half of the radiated energy. The energy flux going through the 30 km radius hemisphere surrounding the Northridge fault is shown in Figure 15. The total work done by seismic waves against the hemisphere is 6.6×10^{14} J. The total static work is 2.1×10^{13} J, only 3.18% of the total work. This small value means the distribution of energy flux on the hemisphere is a fairly accurate representation of the radiated energy even though the hemisphere is not very far from the fault. The static field is small because the Northridge fault did not break the surface. The total radiated energy on the hemisphere is 106% of the total radiated energy on the fault. The ratio is slightly larger than 1.0 largely due to the reflections of seismic waves from the imperfect absorbing boundaries.

[43] It is clear that the energy flux on the hemisphere is very heterogeneous. There are three cones of energy concentration on the sphere, each of which corresponds to one of the three slip pulses (A, B, and C in Figure 12) during the rupture process. Again, the directivity has a major effect. The horizontal thin lines on the hemisphere correspond to the large energy flux trapped along the layer interfaces (Table 4). Owing to the small thickness of the first layer of the velocity profile, the layer interface at the depth of 0.5 km is indistinguishable from the free surface. The layer interfaces at the depths of 1.5 km, 4 km, and 27 km can be clearly seen.

5. Discussion

[44] While it has long been known that directivity could significantly affect the estimate of seismic energy [*Venkataraman and Kanamori*, 2004], the correction for directivity is often omitted or improperly considered by averaging the energy estimates from a number of stations which sample only a small portion of the focal sphere. The underlying assumption for the averaging is that the energy flux distribution on the focal sphere is that derived from a double-couple point source. However, our dynamic simulations of the three finite fault hypothetical events and the Northridge earthquake have shown that the energy flux is highly heterogeneous in the far field with directivity having a major effect. It is unlikely that a simple averaging scheme based on a double-couple radiation pattern would work for this problem.

[45] *Venkataraman and Kanamori* [2004] were the first to attempt correcting explicitly for the directivity effect. They introduced a directivity correction factor, which is determined from the kinematic source model. For a given station distribution, they calculate the synthetics and estimate seismic energy from the synthetics (E_{syn}). They also calculate the total radiated energy from the kinematic source model (E_{source}). The ratio $E_{\text{source}}/E_{\text{syn}}$ is defined as the directivity factor. When this factor is multiplied by the averaged energy estimate from the data (E_{data}) they obtain the final energy estimate. As they note, this directivity factor depends on the kinematic source model used and the station distribution, which limits its use.

[46] Some averaging schemes must be used in estimating seismic energy from the data. This is due to the point source assumption used in current energy estimate schemes. On the basis of this assumption, a single station can estimate the total energy of the earthquake. By averaging energy estimates from a number of stations, a final energy estimate can be obtained. However, this energy estimate depends on the

Table 4. Velocity Structure for the Northridge Earthquake

V_p, m/s	V_s, m/s	Density, kg/m^3	Thickness, km
1900	1000	2100	0.5
4000	2000	2400	1.0
4700	2700	2600	2.5
6300	3600	2800	23.0
6800	3900	2900	13.0
7800	4500	3300	...

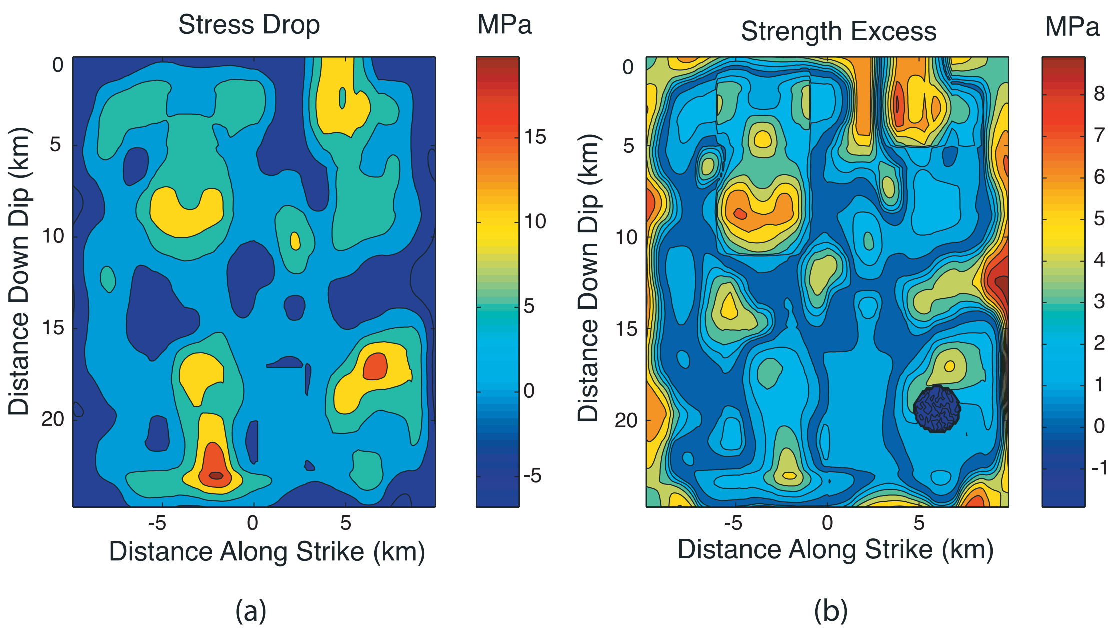

Figure 11. Distributions of (a) the stress drop and (b) the strength excess used in the spontaneous rupture modeling for the Northridge earthquake mapped onto the fault plane.

station distribution. It can be easily seen that one can significantly overestimate or underestimate the seismic energy by using different station distributions that sample a different portions of the focal sphere in Figure 15. This might explain the large discrepancy between teleseismic and regional estimates of radiated energy. Directivity is a finite fault effect. It is not clear how to correct properly for the directivity when using a point source assumption. Unless the distribution of energy flux can be given in a functional form, the correction for directivity is difficult. Thus we infer

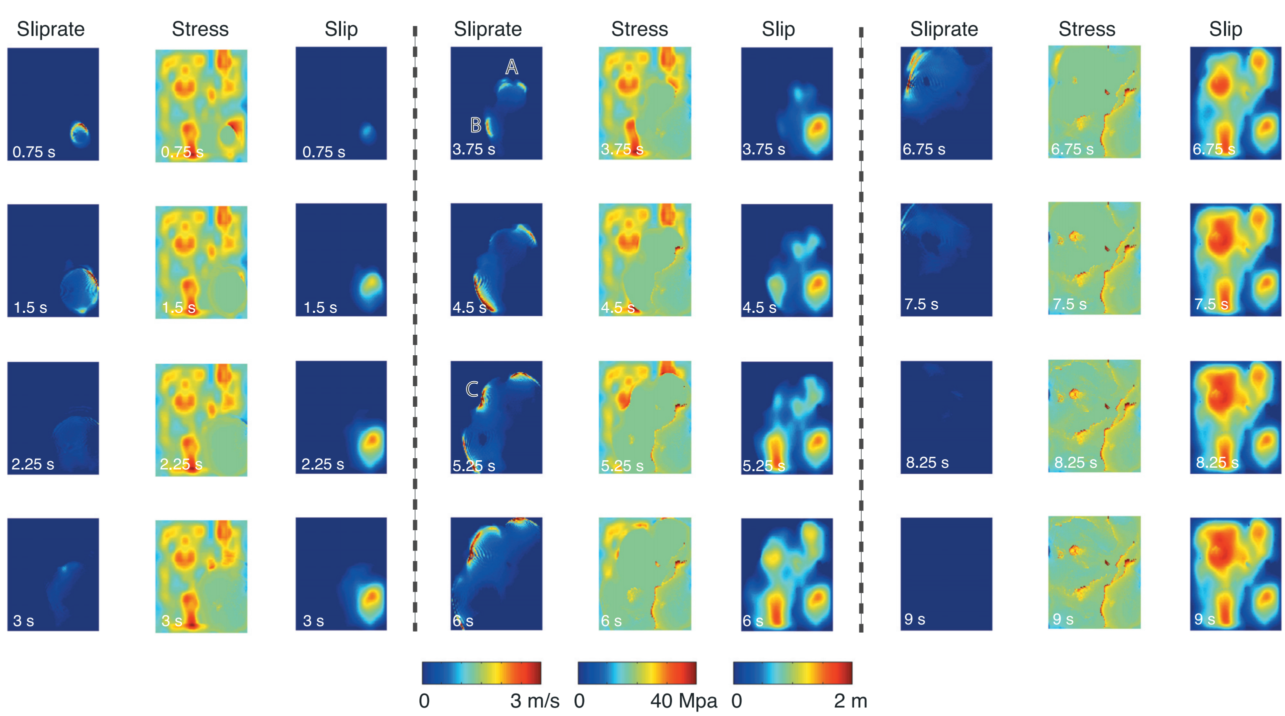

Figure 12. Snapshots of the simulation of the dynamic rupture model for the 1994 Northridge earthquake mapped on the fault plane: showing contours of slip rate, shear stress, and slip at 0.75 s intervals.

Table 5. Strong Motion Stations Used in the Dynamic Simulation of the Northridge Earthquake

Station	Location	Epicentral Distance, km	Azimuth, deg
ARL	Arleta, Nordhoff Avenue fire station	10.24	285.74
ECC	Energy Control Center	20.06	285.45
ENR	Encino, Encino Reservoir Dam	7.45	202.57
MOR	Moorpark	32.01	74.43
NHL	Newhall, Los Angeles County Fire Department	19.58	355.69
PIRU	Lake Piru, Santa Felicia Dam	33.55	34.53
SCS	Sylmar, converting station east	12.70	331.90
SVA	Sepulveda, Veterans Administration hospital	7.78	302.82
SSU	Santa Susana, Department of Energy ground site	15.54	81.75
SYL	Sylmar, county hospital parking lot	15.84	323.66
U06	Sun Valley, 13248 Roscoe	11.57	275.54
U56	Newhall, 26835 W. Pico Canyon	21.15	19.29

that current methods to estimate radiated energy give accurate estimates for large earthquakes only if the directivity effect is minimal.

[47] Estimating energy from a finite fault model, however, can avoid all of these corrections including directivity. From our dynamic simulations of the three hypothetical crustal events, we show that under the same homogeneous stress conditions on the fault surface the reverse fault has the largest apparent stress (0.53 MPa) followed by the strike-slip fault (0.34 MPa) with the normal fault having the smallest apparent stress (0.23 MPa). These results are inconsistent with the mechanism dependence of radiated energy reported by *Choy and Boatwright* [1995] and *Pérez-Campos and Beroza* [2001]. Our results are, however, consistent with the results of *McGarr* [1999] and *Choy and McGarr* [2002] where the apparent stress is directly related to fault strength.

[48] As indicated by *Pérez-Campos and Beroza* [2001], the large discrepancy of energy estimates from teleseismic data and regional data for the same earthquake has to be eliminated before reliable conclusions on the mechanism dependence of radiated energy can be drawn. Indeed, our dynamic simulations show the heterogeneous distributions of energy flux with the largest energy flux concentrated in the forward direction of rupture propagation. A possible explanation for the mechanism dependence of seismic energy suggested by *Pérez-Campos and Beroza* [2001] is that the amount of energy radiated to teleseismic distances is itself mechanism-dependent. However, because each point on the fault radiates, it is not possible to calculate the amount of energy going to teleseismic distances (take-off angles 18°–25°) from the energy flux distribution obtained from our dynamic simulations. Only when the hemisphere is large enough that the fault can be approximated by a point source, can such a calculation be done.

[49] *Choy and Kirby* [2004] provided another possible explanation for the mechanism dependence of radiated seismic energy. They ascribe the differences in apparent stress to fault maturity. Faults that are well developed with a long history of activity, or equivalently faults that have many episodes of slip, are smoother and radiate less seismic energy. They point out that the thrust events analyzed by *Choy and Boatwright* [1995] likely occurred in tectonic environments where the faults could be described as mature. However, the strike-slip and normal faulting earthquakes occurred on immature faults and hence radiated more seismic energy relative to their seismic moment.

[50] From our dynamic model of the 1994 Northridge earthquake we find a radiated energy of 6.0×10^{14} J. This estimate is close to the Gutenberg-Richter estimate of 7.1×10^{14} J and the estimate of *Mayeda and Walter* [1996] at 6.5×10^{14} J, but is roughly two times larger than the NEIC teleseismic estimate (3.1×10^{14} J), and is less than the estimate of 1.3×10^{15} J [*Kanamori and Heaton*, 2000] and 1.2×10^{15} J [*McGarr and Fletcher*, 2002]. It is interesting to note the agreement between our estimate and the estimate of *Mayeda and Walter* [1996], who used coda waves. Coda amplitudes vary little with geology, source radiation anisotropy and directivity. All other estimates do not explicitly correct for the directivity. In a similar study, *Favreau and Archuleta* [2003] estimated the radiated energy for the 1979 Imperial Valley M_w 6.5 earthquake from a spontaneous

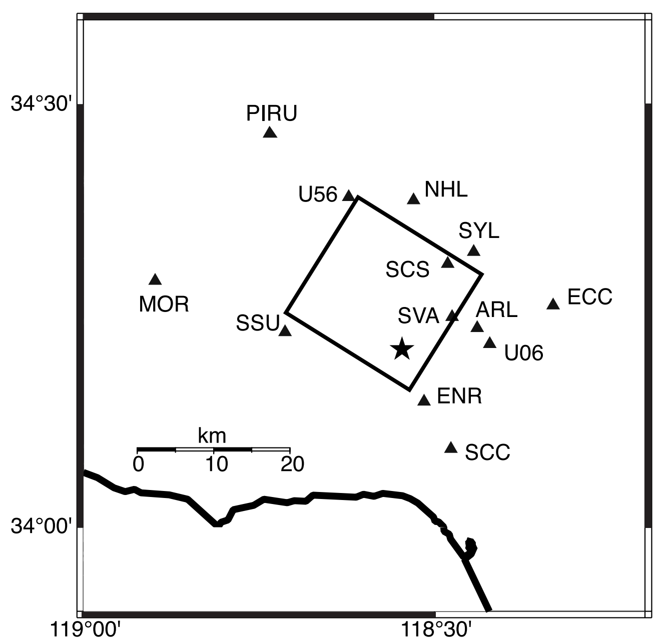

Figure 13. Map of the near-source stations used to constrain the dynamic rupture model. The rectangle depicts the surface projection of the Northridge fault. The star is the epicenter.

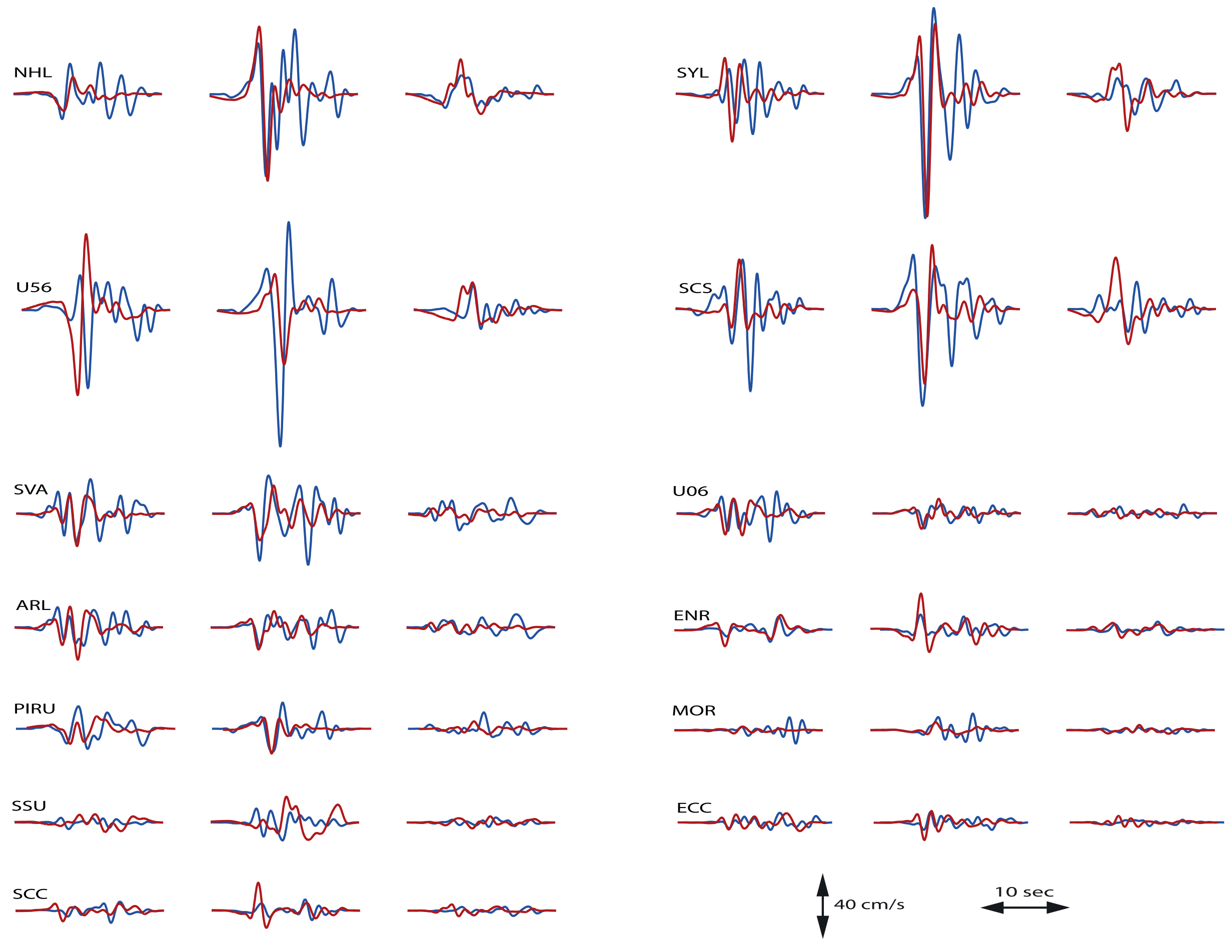

Figure 14. Comparisons of velocity time histories between synthetics (red line) from the dynamic model and near-source ground motions (blue line). For each station the first component is fault-parallel, the second is fault-normal, and the third is vertical. All the synthetics and data are band-pass filtered between 0.1 and 1.0 Hz with a zero-phase, fourth-order Butterworth filter. The scale is the same for all stations so that the rupture directivity of the source can be clearly seen. The overall agreement is good.

dynamic rupture model. They determined the radiated energy for the Imperial Valley earthquake 1.3×10^{14} J with a seismic moment of 7.7×10^{18} Nm (M_w 6.5). The energy-to-moment ratio was 1.7×10^{-5}. The energy-to-moment ratio for the Northridge earthquake from our dynamic model is 4.1×10^{-5}, 2.4 times larger than that of the Imperial Valley earthquake. Although this comparison does not have the statistics of hundreds of earthquakes of *Choy and Boatwright* [1995] and *Pérez-Campos and Beroza* [2001], it is a specific case where a reverse fault radiates more energy than a strike-slip fault.

[51] Near-source ground motions provide a very important constraint on the rupture process. The detailed rupture propagation in the Northridge earthquake has a large effect on the seismic radiation. The heterogeneous energy-flux distribution is largely due to the rupture directivity. For this reason, a dynamic source model constrained by the ground motion data should provide a more accurate and robust energy estimate. Another significant advantage of a dynamic model is the determination of fracture energy, 3.2×10^{14} J for the Northridge earthquake. Our dynamic model shows that the fracture energy in the dynamics of faulting is comparable to the radiated energy and cannot be ignored in the energy balance.

6. Conclusion

[52] Calculating the static field is the key in evaluating the distribution of radiated energy density. Only when the static field is negligible can the distribution of radiated energy density be mapped and uniquely mapped onto a surface. This implies that the mapping of the radiated energy density onto the fault cannot be done and mapping radiated energy onto a distant surface is valid only when the surface is far enough from the fault such that the static field is negligible on the surface.

[53] Dynamic models of three hypothetical events show that the reverse fault has the largest apparent stress (0.53 MPa) compared to that of the strike-slip fault (0.34 MPa) and normal fault (0.23 MPa). The energy-to-moment ratio of

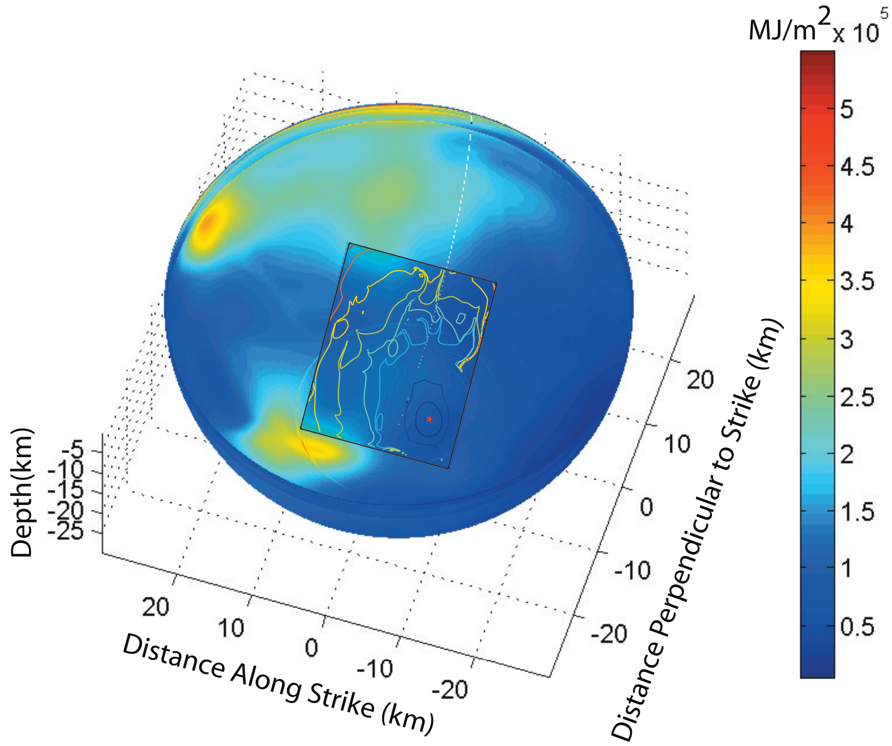

Figure 15. Energy flux distribution on a 30 km radius hemisphere surrounding the Northridge fault. The fault plane with rupture time contours is shown inside the hemisphere. The star is the hypocenter. The origin of the hemisphere is the surface projection of the geometrical center of the fault. Large concentrations of radiated energy are due to the directivity caused by propagation of rupture fronts. The horizontal thin lines on the hemisphere correspond to the high energy flux trapped along the layer interfaces (Table 4). The layer interface at the depth of 0.5 km is indistinguishable from the free surface. The layer interfaces at depths of 1.5 km, 4 km, and 27 km can be clearly seen.

the Northridge M_W 6.7 earthquake (4.1×10^{-5}) is 2.4 times larger than the energy-to-moment ratio of the Imperial Valley M_W 6.6 earthquake (1.7×10^{-5}). This single example differs from the mechanism dependence of radiated energy determined by *Choy and Boatwright* [1995] and *Pérez-Campos and Beroza* [2001]. The uncertainty for current energy estimates is large. The energy flux distribution in the far field shows that large portions of radiated energy are concentrated in the forward direction(s) of propagation. The heterogeneity of the energy flux does not allow simple averaging schemes and emphasizes the difficulties in correcting for directivity in the current energy estimates.

[54] Dynamic faulting models provide an independent and direct estimate of seismic energy. The radiated energy from the spontaneous rupture model of the Northridge earthquake is 6.0×10^{14} J with the energy lost to fracture 3.2×10^{14} J, about one half the radiated seismic energy. By deriving energy from the detailed faulting process, a data-consistent dynamic source model can provide a more accurate and robust estimate of radiated energy.

[55] **Acknowledgments.** We thank Steve Hartzell for sending the Northridge inversion results. We are grateful to Pengcheng Liu, Eric Dunham, and Morgan Page for many useful discussions. We appreciate the insightful comments of George Choy. Morgan Page's revision of a draft of this paper greatly improved the manuscript. Two anonymous reviewers gave very constructive reviews. This work was supported by the Keck Foundation, which established an Interdisciplinary Program in Seismology and Materials Physics at UCSB, by the Southern California Earthquake Center (SCEC), by NSF under contract EAR-0122464 (The SCEC Community Modeling Environment (SCEC/CME): An Information Infrastructure for System-Level Earthquake Research), and by an IGPP/LANL grant 04-08-16L-1532. SCEC is funded by NSF Cooperative Agreement EAR-0106924 and USGS Cooperative Agreement 02HQAG0008. This is SCEC contribution number 949 and Institute for Crustal Studies contribution number 0729.

References

Andrews, D. J. (1999), Test of two methods for faulting in finite-difference calculations, *Bull. Seismol. Soc. Am.*, *89*, 931–937.

Beroza, G., and T. Mikumo (1996), Short slip duration in dynamic rupture in the presence of heterogeneous fault properties, *J. Geophys. Res.*, *101*, 22,449–22,460.

Boatwright, J., and G. L. Choy (1986), Teleseismic estimates of the energy radiated by shallow earthquakes, *J. Geophys. Res.*, *91*, 2095–2112.

Boatwright, J., G. L. Choy, and L. C. Seekins (2002), Regional estimates of radiated seismic energy, *Bull. Seismol. Soc. Am.*, *92*, 1241–1255.

Bouchon, M. (1997), The state of stress on some faults of the San Andreas system as inferred from near-field strong motion data, *J. Geophys. Res.*, *102*, 11,731–11,744.

Choy, G. L., and J. Boatwright (1995), Global patterns of radiated seismic energy and apparent stress, *J. Geophys. Res.*, *100*, 18,205–18,228.

Choy, G. L., and S. H. Kirby (2004), Apparent stress, fault maturity and seismic hazard for normal-fault earthquakes at subduction zones, *Geophys. J. Int.*, *159*, 991–1012.

Choy, G. L., and A. McGarr (2002), Strike-slip earthquakes in the oceanic lithosphere: Observations of exceptionally high apparent stress, *Geophys. J. Int.*, *150*, 506–523.

Day, S. M., G. Yu, and D. J. Wald (1998), Dynamic stress changes during earthquake rupture, *Bull. Seismol. Soc. Am.*, *88*, 512–522.

Dreger, D. S. (1994), Empirical Green's function study of the January 17, 1994, Northridge, California earthquake, *Geophys. Res. Lett.*, *21*, 2633–2636.

Favreau, P., and R. J. Archuleta (2003), Direct seismic energy modeling and application to the 1979 Imperial Valley earthquake, *Geophys. Res. Lett.*, *30*(5), 1198, doi:10.1029/2002GL015968.

Fukuyama, E. (2005), Radiation energy measured at earthquake source, *Geophys. Res. Lett.*, *32*, L13308, doi:10.1029/2005GL022698.

Gutenberg, B. (1942), Earthquake magnitude, intensity, energy, and acceleration, *Bull. Seismol. Soc. Am.*, *32*, 163–191.

Gutenberg, B., and C. R. Richter (1956a), Earthquake magnitude, intensity, energy, and acceleration, *Bull. Seismol. Soc. Am.*, *46*, 105–145.

Gutenberg, B., and C. F. Richter (1956b), Magnitude and energy of earthquakes, *Ann. Geofis.*, *9*, 1–15.

Hartzell, S. H., P.-C. Liu, and C. Mendoza (1996), The 1994 Northridge earthquake: Investigation of rupture velocity, rise time and high-frequency radiation, *J. Geophys. Res.*, *101*, 20,091–20,108.

Haskell, N. (1964), Total energy and energy spectral density of elastic wave radiation from propagating faults, *Bull. Seismol. Soc. Am.*, *56*, 1811–1842.

Houston, H. (1990), Broadband source spectrum, seismic energy, and stress drop of the 1989 Macquarie Ridge earthquake, *Geophys. Res. Lett.*, *17*, 1021–1024.

Houston, H., and H. Kanamori (1990), Comparison of strong motion spectra with teleseismic spectra for three magnitude 8 subduction-zone earthquakes, *Bull. Seismol. Soc. Am.*, *80*, 913–934.

Ida, Y. (1972), Cohesive force across the tip of a longitudinal-shear crack and Griffith's specific surface energy, *J. Geophys. Res.*, *77*, 3796–3805.

Ide, S. (2002), Estimation of radiated energy of finite-source earthquake models, *Bull. Seismol. Soc. Am.*, *92*, 2994–3005.

Kanamori, H., and D. L. Anderson (1975), Theoretical basis of some empirical relations in seismology, *Bull. Seismol. Soc. Am.*, *65*, 1073–1095.

Kanamori, H., and T. Heaton (2000), Microscopic and macroscopic mechanisms of earthquakes, in *GeoComplexity and the Physics of Earthquakes*, *Geophys. Monogr. Ser.*, vol. 120, edited by J. B. Rundle, D. L. Turcotte, and W. Klein, pp. 147–163, AGU, Washington, D. C.

Kanamori, H., E. Hauksson, L. K. Hutton, and L. M. Jones (1993), Determination of earthquake energy release and M_L using TERRAscope, *Bull. Seismol. Soc. Am.*, *78*, 1707–1724.

Kikuchi, M., and Y. Fukao (1988), Seismic wave energy inferred from long-period body wave inversion, *Bull. Seismol. Soc. Am.*, *78*, 1707–1724.

Kostrov, B. V. (1974), Seismic moment and energy of earthquakes and seismic flow of rock, *Izv. Earth Phys.*, *1*, 23–40.

Lysmer, J., and R. L. Kuhlemeyer (1969), Finite dynamic model for infinite media, *J. Eng. Mech.*, *95*, 859–877.

Madariaga, R. (1977), High-frequency radiation from crack (stress drop) models of earthquake faulting, *Geophys. J. R. Astron. Soc.*, *51*, 625–651.

Mayeda, K., and W. R. Walter (1996), Moment, energy, stress drop, and source spectra of western United States earthquakes from regional coda envelopes, *J. Geophys. Res.*, *101*, 11,195–11,208.

McGarr, A. (1980), Some constraints on levels of shear stress in the crust from observations and theory, *J. Geophys. Res.*, *85*, 6231–6238.

McGarr, A. (1999), On relating apparent stress to the stress causing earthquake fault slip, *J. Geophys. Res.*, *104*, 3003–3011.

McGarr, A., and J. B. Fletcher (2002), Mapping apparent stress and energy radiation over fault zones of major earthquakes, *Bull. Seismol. Soc. Am.*, *92*, 1633–1646.

McGarr, A., and N. C. Gay (1978), State of stress in the Earth's crust, *Ann. Rev. Earth Planet. Sci.*, *6*, 405–436.

Nielsen, S. B., and K. B. Olsen (2000), Constraints on stress and friction from dynamic rupture models of the 1994 Northridge, California, earthquake, *Pure Appl. Geophys.*, *157*, 2029–2046.

Oglesby, D. D., R. J. Archuleta, and S. B. Nielsen (1998), Earthquakes on dipping faults: The effects of broken symmetry, *Science*, *280*, 1055–1059.

Pérez-Campos, X., and G. C. Beroza (2001), An apparent mechanism dependence of radiated seismic energy, *J. Geophys. Res.*, *106*, 11,127–11,136.

Peyrat, S., K. Olsen, and R. Madariaga (2001), Dynamic modeling of the 1992 Landers earthquake, *J. Geophys. Res.*, *106*, 26,467–26,482.

Rivera, L., and H. Kanamori (2005), Representations of the radiated energy in earthquakes, *Geophys. J. Int.*, *162*, 148–155, doi:10.1111/j.1365-246X.2005.02648.x.

Scholz, C. H. (2002), *The Mechanics of Earthquakes and Faulting*, Cambridge Univ. Press, New York.

Singh, S. K., and M. Ordaz (1994), Seismic energy release in Mexican subduction zone earthquakes, *Bull. Seismol. Soc. Am.*, *84*, 1533–1550.

Vassiliou, M. S., and H. Kanamori (1982), The energy release in earthquakes, *Bull. Seismol. Soc. Am.*, *72*, 371–387.

Venkataraman, A., and H. Kanamori (2004), Effect of directivity on estimates of radiated seismic energy, *J. Geophys. Res.*, *109*, B04301, doi:10.1029/2003JB002548.

Venkataraman, A., L. Rivera, and H. Kanamori (2002), Radiated energy from the 16 October 1999 Hector Mine earthquake: Regional and teleseismic estimates, *Bull. Seismol. Soc. Am.*, *92*, 1256–1265.

Wald, D. J., T. H. Heaton, and K. W. Hudnut (1996), The slip history of the 1994 Northridge, California, earthquake determined from strong-motion, teleseismic, GPS, and leveling data, *Bull. Seismol. Soc. Am.*, *86*, S49–S70.

Winslow, N. W., and L. J. Ruff (1999), A hybrid method for calculating the radiated wave energy of deep earthquakes, *Phys. Earth Planet. Inter.*, *116*, 181–190.

Wyss, M., and J. Brune (1971), Regional variations of source properties in southern California estimated from the ratio of short- to long-period amplitudes, *Bull. Seismol. Soc. Am.*, *61*, 1153–1168.

Zeng, Y., and J. G. Anderson (1996), A composite source modeling of the 1994 Northridge earthquake using genetic algorithm, *Bull. Seismol. Soc. Am.*, *86*, S71–S83.

R. J. Archuleta and S. Ma, Department of Earth Science, University of California, Santa Barbara, CA 93106, USA. (sma@crustal.ucsb.edu)